Elastic imaging with OBS receiver-side multiples

Yuting Duan & Paul Sava
Center for Wave Phenomena, Colorado School of Mines

ABSTRACT

Receiver-side water-column multiples acquired with ocean-bottom seismic sensors can be used for elastic imaging of the subsurface, which can provide additional information relative to more conventional acoustic imaging. These multiples can be separated from primaries contained in ocean-bottom seismic data using techniques such as up/down decomposition. In elastic imaging, the down-going wavefield consists of only P-waves because multiples propagate through the water-column. Receiver-side water-column multiples can be imaged by backpropagation from virtual receivers located at symmetric positions relative to the ocean surface, thereby increasing the imaging aperture. We perform imaging in the angle domain, which enables us to reverse the reflection polarity change at normal incidence. In addition to physical reflections, a strong solid/liquid interface at the ocean bottom generates unwanted mode conversions which are present in the images in the form of cross-talk between physical and non-physical events. However, this cross-talk can be easily identified in shot-domain or image-domain common-image gathers, and can therefore be removed after imaging. In the end, our procedure leads to a collection of images accounting for different combinations of incident and reflected P and S waves. These images exploit surface-related multiples, and are therefore the expression of different subsurface illumination relative to the analogous reflections using primary reflections only. Such elastic images can be used to infer accurate lithological information about the subsurface using angle-dependent reflectivity for different combinations of incident and reflected waves.

Key words: elastic wavefields, reverse-time migration, OBS

1 INTRODUCTION

Seismic data acquisition using ocean-bottom seismic (OBS) sensors is a rapidly developing technology that can address significant challenges in marine acquisition. For example, OBS acquisition can provide wide-azimuth recording geometries (Dash et al., 2009). Typical OBS systems consist of a hydrophone and a geophone that record pressure and three components of particle velocity, respectively. In contrast to more conventional acquisition geometries, OBS acquisition typically consists of a sparse set of receivers on the ocean bottom and a relatively dense network of sources at the ocean surface. The OBS sensors are sparsely distributed on the ocean bottom due to their high cost and also to the difficulty of their deployment. However, the small number of OBS sensors is compensated for by a dense network of sources at the ocean surface. This setup enables acquisition of wide-azimuth data, which is invaluable in imaging complex geologic structures (Grion et al., 2007; Dash et al., 2009; Berg et al., 2010; Wong et al., 2011). Furthermore, four-component data acquisition facilitates separation of acquired data into up-going and down-going waves, as well as into P- and S-modes (Schalkwijk, 2001). This separation enables imaging of the subsurface using elastic waves, which can potentially provide access to lithological information.

Although usually strong, receiver-side first-order water-column multiples are often considered noise and removed from the acquired data, after which imaging is performed using primaries separated at the ocean bottom. However, multiples contain additional information beyond primaries and provide increased illumination of the subsurface (Ronen et al., 2005; Dash et al., 2009; Tu et al., 2011; O'Brien et al., 2013). Imaging using multiples can be carried out by assuming that receivers are located on a virtual horizon that mirrors the ocean bottom across the ocean surface (Ronen et al., 2005; Dash et al., 2009; Wong et al., 2011). These multiples provide a wider illumination of the subsurface, especially in deep water.

OBS imaging with receiver-side water-column multiples is usually performed under the acoustic assumption. In this paper, we develop a method for elastic imaging with OBS data in order to generate images of the subsurface using both P-

and S-modes separated from receiver-side water-column multiples. For this purpose, we first make use of the fact that the P-modes propagating into the water column convert to S-modes when crossing the ocean bottom. Then, we perform elastic reverse-time migration (RTM) using an imaging condition based on wave-mode separation with Helmholtz decomposition (Dellinger and Etgen, 1990; Yan and Sava, 2008) to produce images corresponding to all possible combinations of P- and S-modes extracted from the source and receiver wavefields.

Our methodology relies on mode conversions at the ocean bottom in order to use converted waves for imaging. We reconstruct the receiver wavefield using the down-going waves observed in the recorded data. In the reconstructed receiver wavefield, some P-to-S conversions at the ocean bottom correspond to physical events, i.e., the ray paths of the conversions can be tracked in the reconstructed source wavefield. However, other P-to-S conversions are not physical, but are merely artifacts of the elastic wavefield extrapolation used in migration. These non-physical conversions generate artifacts in the image that interfere with the true geologic reflectors in the subsurface and, therefore, look similar to the artifacts due to multiples or crosstalk between separate physical experiments. However, the spatial positions of these artifacts are not consistent in images computed for different shot positions, and thus they can be identified in common-image gathers (CIGs) and can be differentiated from physical reflection events by their nonzero moveout.

The novelty of our paper is that we combine related methods to solve the problems that occur in elastic migration with OBS water-column multiples in order to improve the quality of the image. In the following sections, we describe the sequence of steps necessary for elastic migration using water-column multiples, and then we illustrate our methodology with a modified Marmousi model.

2 THEORY

Our procedure for elastic imaging using water-column multiples consists of several steps, as outlined here. First, we decompose the recorded data into up- and down-going waves in order to isolate the water-column multiples. We then apply elastic imaging and compute PS and SP angle gathers to reverse the reflectivity polarity change across images obtained for different experiments. Finally, we remove artifacts caused by wave-mode conversions at the ocean bottom and the sparse receiver geometry. In the following, we detail our specific implementation.

2.1 Up/down separation

An OBS seismometer contains a hydrophone that records the scalar pressure field as well as a geophone that records three components of particle velocity (Berg et al., 2010). The pressure represents the spatial derivatives of the particle displacement, while the velocity represents the time derivatives of the displacement. With this information, four-component OBS data provides the ability to decompose the wavefield into primaries and multiples at the receiver locations. Following wavefield decomposition, we can use the separated multiples and primaries for migration. In our paper, we focus only on migration with multiples.

Wavefield decomposition methods can be classified into two general categories: (1) methods based on theoretical analysis of wave equations at a liquid-solid boundary, and (2) methods that predict multiples from primary reflections. Techniques in the first category usually make certain assumptions in order to obtain a computationally efficient expression for the mutiple and primary separation (Barr and Sanders, 1989; Amundsen and Reitan, 1995; Osen and Amundsen, 2001; Schalkwijk, 2001). For example, Barr and Sanders (1989) assume that the reflection and transmission coefficients are known, and Amundsen and Reitan (1995) use the plane-wave assumption . The second category of methods can predict both source- and receiver-side water-column multiples in OBS data (Xia et al., 2006; Ma et al., 2010; Jin and Wang, 2012) under certain assumptions. For example, one could assume that the amplitude of the direct arrivals is preserved following preprocessing procedures (Ma et al., 2010) or that the wavefield is densely recorded or interpolated in both the receiver and shot grids (Jin and Wang, 2012).

Our method belongs in the first category and uses PZ summation. The term PZ summation refers to the summation and subtraction of the P (pressure) and Z (the vertical velocity) data, after appropriate weighting, to compute up- and down-going waves, respectively. Assuming that the ocean bottom is horizontal, receiver-side water-layer multiples are down-going waves propagating toward the ocean bottom in the water layer, while primaries propagate upward toward the ocean bottom. Also, down-going waves in pressure data have opposite polarity compared to down-going waves in vertical velocity data. These different characteristics of up-going (U) and down-going (D) waves allow for their separation using these expressions (Grion et al., 2007):

$$U = \frac{1}{2}P + \alpha\, V_z\ , \tag{1}$$

$$D = \frac{1}{2}P - \alpha\, V_z\ , \tag{2}$$

where P and V_z represent the vertical component of the pressure and particle velocity vector, respectively, and α is a scale factor that depends on certain assumptions, e.g., that the OB reflectivity is known (Schalkwijk, 2001; Xia et al., 2006) or that the amplitudes of hydrophone and geophone traces are not affected by the data processing procedures prior to wavefield decomposition (Hoffe et al., 1999).

We demonstrate up/down separation, in addition to other procedures discussed below, using the synthetic model shown in Figures 1(a)-1(c), which contains one horizontal reflector in the subsurface below the ocean bottom. Our acquisition geometry is designed to be similar to that of a typical OBS survey, and consists of 11 receivers sparsely located on the ocean bottom at $z = 0.8$ km and 91 sources evenly distributed along the ocean surface. Figure 2(a) shows a shot gather contain-

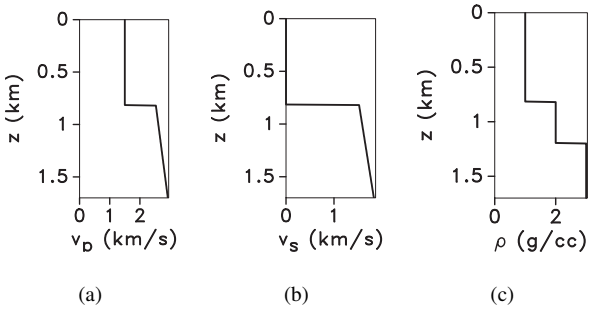


Figure 1. The 2D test model; (a) P-wave velocity (b) S-wave velocity and (c) density profiles in the 2D synthetic model.

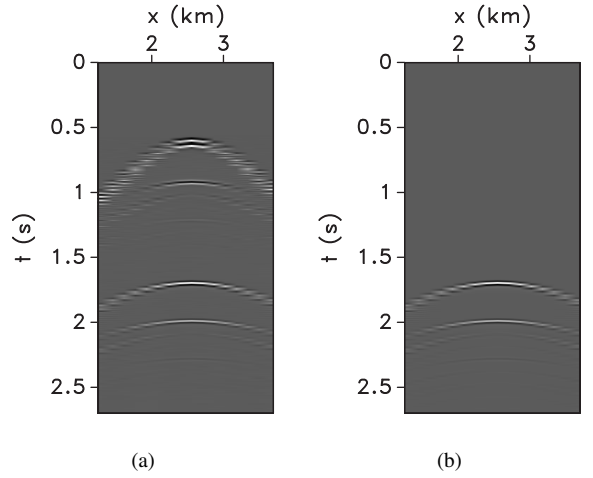


Figure 2. (a) A shot gather containing up- and down-going waves; (b) The decomposed down-going waves.

ing direct waves, primary reflections, internal multiples, and water-column multiples. After up/down separation, we obtain only the down-going waves (Figure 2(b)), which represent the receiver-side water-column multiples.

Note that both up- and down-going modes may potentially contain other multiples (higher-order surface-related multiples or internal multiples). However, we assume that these multiples are lower in amplitude and thus do not significantly contribute to the migration image. This is, of course, a limitation of our method. If this assumption is violated in practice, then the migration images will be contaminated by additional cross-talk noise, similar to the case discussed later in this paper.

2.2 Mirror imaging

For typical OBS acquisition geometries, nodes are usually sparsely distributed on the ocean bottom due in part to their high cost as well as to their difficulty of deployment. With this acquisition geometry, receiver-side water-column multiples can provide wider angles of illumination than primaries (Dash et al., 2009). For example, comparing water-column multiples to primary reflections from the same reflector, the multiples propagate an additional distance through the water column, and thus are able to reach receivers at locations farther than those reached by the primary reflections, as shown in Figure 3 .

We use mirror imaging to migrate water-column multiples (e.g., Pica et al., 2006; Wong et al., 2011). With this method, we first separate water-column multiples from primary reflections, and then we compute the receiver-side wavefield by back propagating only the water-column multiples from virtual receivers located at positions symmetric to their physical locations across the ocean surface, i.e., we mirror the receivers across the ocean surface. Note that when separately migrating primary reflections and water-column multiples using mirror imaging, we use an absorbing boundary condition rather than a free-surface boundary condition in order to avoid unwanted reflections at the ocean surface. Also, note that separated water-column multiples contain first-order multiples as well as higher-order multiples. Mirror imaging can also be used to image higher-order multiples (e.g., Wong et al., 2011), but in this paper we consider only the first-order multiples, and we regard higher-order multiples as noise, as such waves typically are much weaker in amplitude compared to first-order multiples.

2.3 Imaging condition

Reconstructed source and receiver elastic wavefields can be separated into P- and S-modes prior to imaging (Dellinger and Etgen, 1990; Yan and Sava, 2008). In isotropic media, this separation can be achieved using the Helmholtz decomposition theorem (Aki and Richards, 2002), which describes the P- and S-modes in terms of the displacement vector $\mathbf{u}(\mathbf{x}, t)$:

$$P = \nabla \cdot \mathbf{u} \,, \tag{3}$$

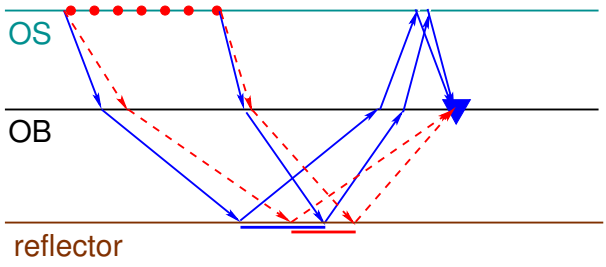
$$\mathbf{S} = \nabla \times \mathbf{u} \,. \tag{4}$$

In isotropic media, the S-mode consists of two degenerate waves which are indistinguishable from one-another. In the case of 2D wave propagation, the S-mode has only one nonzero component, and thus can be treated as a scalar. We can then use the imaging condition formulated by Yan and Sava (2008) to combine different wave-modes from source and receiver wavefields to obtain independent images for different combinations of incident and reflected wave modes:

$$R^{ij}(\mathbf{x}, t) = \sum_t {W_s}^i(\mathbf{x}, t)\, {W_r}^j(\mathbf{x}, t) \;. \tag{5}$$

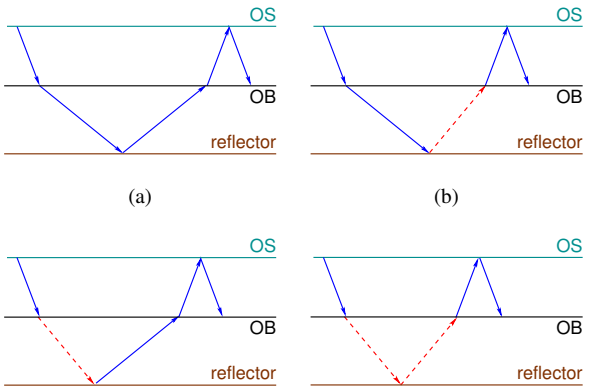
Here, indices i and j indicate the wave-mode used in imaging.

Figures 5(a)-6(b) show PP, SS, PS, and SP images computed from all the shots using mirror imaging, i.e., with receiver multiples back propagated from virtual receivers mirrored across the ocean surface. For all images in Figures 5(a)-6(b), we observe the reflector at its true depth of $z = 1.2$ km, but we also observe cross-talk artifacts due to interference between non-physical P- and S-modes. However, separating the true reflection events from cross-talk artifacts is not triv-



(a)

Figure 3. Different illumination patterns in the subsurface for primary (dashed lines) and water layer multiples (solid lines).



(a) (b)

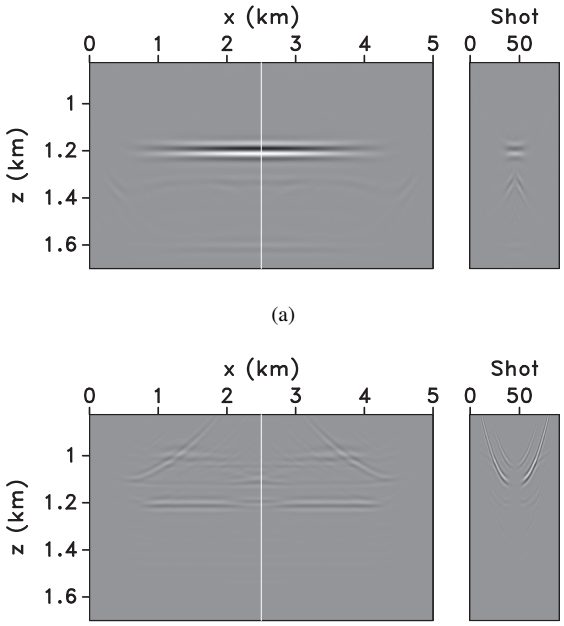
(c) (d)

Figure 4. Schematic representation of the receiver-side first-order surface-related multiples. The solid lines represent P-waves and the dashed lines represent S-waves. From (a) to (d), the panels correspond to PP, PS, SP and SS reflections.

ial, as the artifacts can be stronger in amplitude than the true events. For example, in Figure 5(b), the true reflector (at depth $z = 1.2$ km) is difficult to distinguish from the much stronger artifacts. Also, notice in the PS and SP images shown in Figure 6(a) and 6(b), respectively, that the reflector is less coherent near the center of the model. This lack of coherence is due to the change in sign of PS and SP reflection coefficients across normal incidence. By stacking over all shots, some of the migrated images have opposite polarity and interfere destructively. In the next sections, we discuss how to deal with polarity change, and attenuate the cross-talk artifacts.

2.4 Polarity reversal

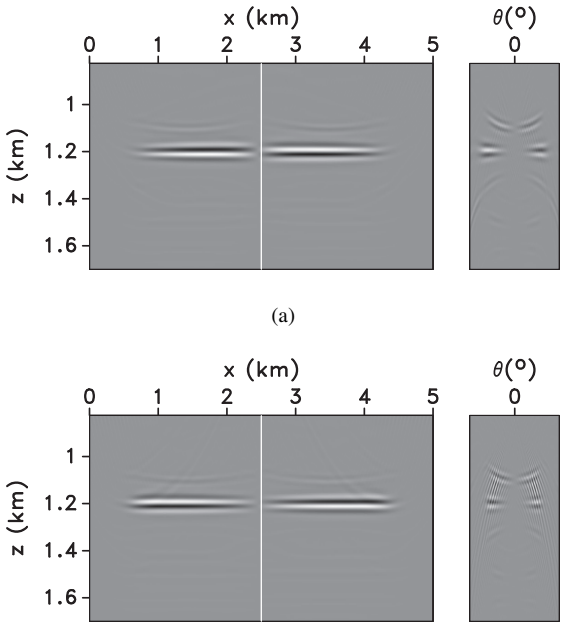
In isotropic media, the signs of PS and SP reflection coefficients change across normal incidence. Additional sign changes can occur at large angles of incidence, but in isotropic media, energy reflected at large incidence angles is generally



(a)

(b)

Figure 5. The (a) PP and (b) SS migrated images of the OBS receiver-side multiples. The vertical line on the migrated image indicates the position of the shot-domain CIGs.



(a)

(b)

Figure 6. (a) PS and (b) SP migrated images of the OBS receiver-side multiples. The vertical line on the migrated image indicates the position of the angle-domain CIGs.

weaker, so the effects of these additional sign changes are negligible. The normal incidence change can be observed in angle-domain CIGs. For the synthetic model shown in Figures 1(a)-1(c), we obtain the PS and SP images shown in Figures 6(a) and 6(b), respectively, by applying the imaging condition in equation 5. Polarity reversal can be performed using ray theory (Balch and Erdemir, 1994), wavenumber-domain separation (Du et al., 2011), or angle-domain imaging conditions (Yan and Sava, 2008; Du et al., 2011; Yan and Xie, 2012). In this paper, we follow Yan and Sava (2008) and reverse the polarity change for PS and SP images in the angle-domain. To obtain angle-domain CIGs, we first compute space-lag extended images (Rickett and Sava, 2002; Sava and Vasconcelos, 2009):

$$R_e^{ij}(\mathbf{x},\boldsymbol{\lambda}) = \sum_t W_s^i(\mathbf{x}-\boldsymbol{\lambda},t)\, W_r^j(\mathbf{x}+\boldsymbol{\lambda},t)\ . \quad (6)$$

Here, $\mathbf{x} = \{x, y, z\}$ represents the space coordinates and $\boldsymbol{\lambda} = \{\lambda_x, \lambda_y, \lambda_z\}$ represents the space-lag vector. Then, we map the extended images to the angle domain $R_e^{ij}(\mathbf{x}, \theta, \phi)$ using conventional methods (Sava and Fomel, 2003; Sava and Vlad, 2011). As discussed by Sava and Vlad (2011), it is not necessary to compute all space lags in order to obtain the opening angle θ and azimuth angle ϕ. We can compute just two of the three space lags and then reconstruct the third lag with the given reflector normal.

The right panels of Figures 6(a) and 6(b) show angle gathers for the synthetic model (Figures 1(a)-1(c)) at $x = 3.0$ km after we reverse the polarity changes for PS and SP reflections, respectively. After applying the polarity reversal at each image point, we obtain the PS and SP images (Figures 6(a) and 6(b)) by stacking over angle gathers.

However, even after polarity reversal, the angle gathers (right panels of Figures 6(a) and 6(b)) still contain artifacts due to the sparse distribution of receivers and the non-physical wave conversions. These artifacts might stack out during imaging, but we choose to eliminate them so that we can, for example, better use the gathers for velocity analysis. The following section details how we remove the sampling artifacts.

2.5 Artifact attenuation

Elastic reverse-time migration requires numerical reconstruction of source and receiver wavefields. For the source wavefield, we simulate an elastic wavefield using a pressure source located at a known position near the surface. For the receiver-side wavefield, we simulate an elastic wavefield by using the recorded data, separated into primaries and multiples, as sources in the water column. Injected P-modes not only propagate through the ocean bottom as P-modes, but also convert into S-modes as they cross the liquid-solid interface. Some conversions correspond to physical S-modes that originate from reflectors in the subsurface, but other non-physical conversions lead to fake modes that do not represent wave propagation. Such fake modes produce artifacts in the migrated images. For example, in Figure 5(b), notice the artifacts

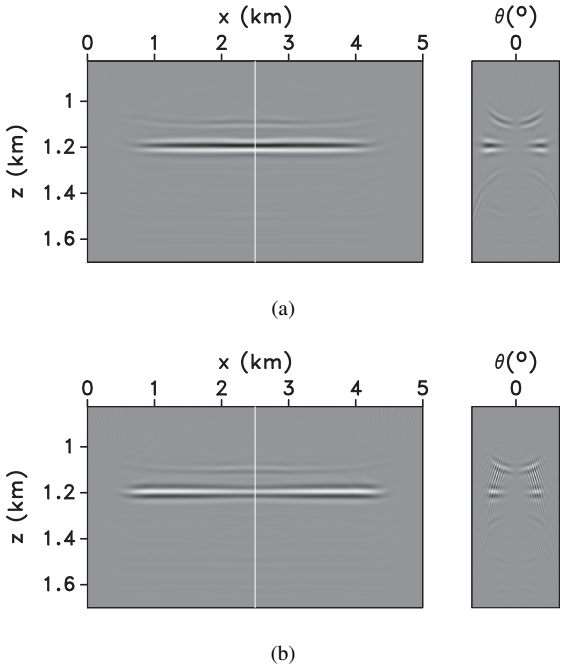


Figure 7. The (a) PS and (b) SP images after polarity correction. The vertical line on the image indicates the position of the angle-domain CIGs which are on the right panel.

that are apparent above the true reflector location (at depth $z = 1.2$ km).

OBS acquisition geometry contains sparse receivers, which result in artifacts in the migrated images. Stacking over a dense network of shots is an effective way to reduce the artifacts and improve the signal-to-noise ratio. However, the reflector amplitude may decrease after stacking due to the presence of artifacts. These artifacts are generally inconsistent between different shots and across different incidence angles; therefore, they appear as events with anomalous move-out in gathers where they can be attenuated using different techniques, e.g., using Radon transforms (Sava and Guitton, 2005) or plane-wave destruction filters (Fomel, 2002). Such techniques assume that the velocity model used for imaging is accurate, so that the true reflection events are flat as a function of shot number or incidence angle, even when polarity changes exist, which is the case for PS and SP images. This artifact attenuation is necessary, since some artifacts can be significantly stronger than true reflection events. For example, a weak SS reflection can easily be overwhelmed by artifacts caused by fake PS, SP, or even PP reflections.

The depths of fake events are inconsistent with respect to shot location and incidence angle; therefore, in order to remove such artifacts, we must remove non-flat events in CIGs while preserving the amplitudes of flat events. This artifact attenuation can be implemented, for example, in the wavenumber domain using an f-k filter (Stewart and Schieck, 1989) that passes energy around $k_z = 0$ and attenuates energy at $k_z \neq 0$. In practice, however, we cannot achieve an ideal filter with

a sharp boundary in the wavenumber domain because such a filter has infinite extent in the original (CIG) domain. To obtain a finite-extent impulse response in the original domain, we window the ideal impulse response using a Hamming window (Oppenheim and Schafer, 2009).

The right panels of Figures 5(a) and 5(b) show the PP and SS shot-domain CIGs, respectively, at $x = 2.5$ km in the 2D synthetic model (Figures 1(a)-1(c)). As seen in the shot-domain CIGs — for example, a PP shot-domain CIG (left panel of Figure 8(a)) — the true reflection is characterized by a flat event as a function of shot number, while the artifacts appear as events with nonzero moveout. The corresponding CIG in the wavenumber domain for PP shot-domain CIGs is shown in the right panel of Figure 8(a). Notice that the energy of flat events is focused around $k_z = 0$. After we apply the f-k filter, only the events focused around $k_z = 0$ are preserved, as shown in Figure 8(b). Figures 9(a) and 9(b) show the PP and SS shot-domain CIGs after artifact attenuation. Choosing a proper filter in the wavenumber domain is tricky. On the one hand, we want the filter to be narrow enough to attenuate even those events with small moveout and still preserve the flat events. On the other hand, we know that the filter will cause smear effect and thus blurs edges of the events which will change the amplitude of the events. Therefore, it is important to choose a proper width for the f-k filter.

Similarly, in PS and SP angle-domain CIGs, the true reflections do not change in depth with incidence angle (right panels of Figures 6(a) and 6(b)). Therefore, we can also employ an f-k filter to attenuate crosstalk artifacts in the angle domain (Figures 9(c) and 9(d)). The artifacts, however, cannot be completely removed as some are nearly flat. Note that although we use shot-domain CIGs to attenuate artifacts in PP and SS images, we could also use angle-domain CIGs and follow the same artifact attenuation procedure used for PS and SP images.

In summary, receiver-side water-column multiples can be used to generate elastic images. Similar to the acoustic case, we separate receiver-side water-column multiples from primaries in recorded OBS data, and then use mirror imaging to migrate the multiples. However, additional procedures are required in the elastic case, including reversing the polarity changes in PS and SP images and attenuating artifacts caused by non-physical wave-mode conversions. With these additional procedures, we are able to obtain PP, PS, SP, and SS images of the subsurface.

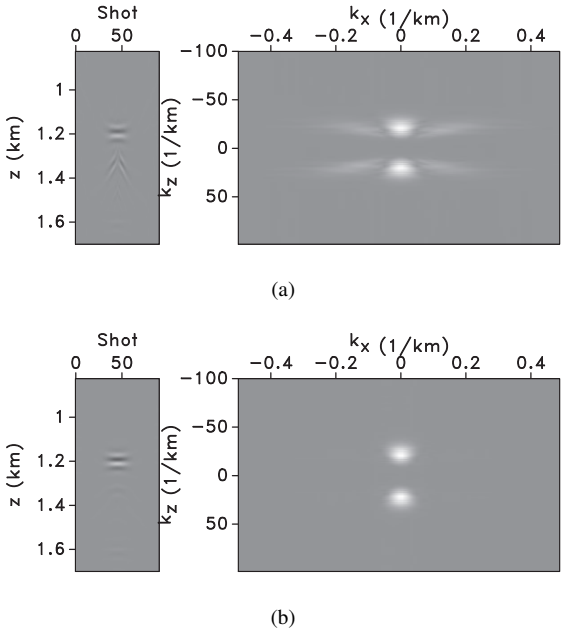


Figure 8. The PP shot-domain CIGs (a) before and (b) after artifact removal. The panels on the right are the corresponding wavenumber domain CIGs of the left panels.

3 EXAMPLES

We demonstrate our method on a modified version of the Marmousi model shown in Figure 10. Compared to the original Marmousi model, our model contains a thicker water layer, which allows for wider illumination when we migrate the down-going waves from receiver-side multiples. The P-wave velocity, S-wave velocity, and density models are shown in the top, middle, and bottom panels of Figure 10, respectively. The ocean bottom is not smooth so as to facilitate wave-mode conversions at the ocean bottom to obtain PP, PS, SP, and SS images.

We generate synthetic data using 290 sources evenly distributed along the ocean surface. The source function is a Ricker wavelet with a peak frequency of 25 Hz. There are 30 receivers sparsely located at the ocean bottom from $x = 1.7$ km to $x = 4.0$ km, as indicated by the dots in Figure 10.

A subset of the PP angle-domain CIGs is shown in the middle panel of Figure 11. As we migrate using the correct velocity, the depths of the imaged reflectors do not change with shot location, and the true reflections appear flat. We apply the f-k filter discussed earlier to attenuate the artifacts in the PP angle-domain CIGs shown in the middle panel of Figure 11. As discussed earlier, this procedure can be carried out either in the angle domain or in the shot domain. For PS and SP images, it is convenient to perform artifact attenuation in the angle domain since polarity correction is also performed in this angle domain. For consistency with the PS and SP imaging, we also perform artifact attenuation in the angle domain for PP and SS images. After artifact attenuation, the gathers contain only flat events, indicating that the cross-talk artifacts have been attenuated and that the reflectors are correctly positioned in the subsurface.

We use the same f-k filter to attenuate artifacts in the SS angle-domain CIGs shown in the middle panel of Figure 14. In these CIGs, there are fewer and weaker reflections compared to the PP angle-domain CIGs (middle panel of Figure 11), as SS angle-domain CIGs are computed using the S-modes in the source and receiver wavefields, and the incident S-modes are converted at the water bottom.

The PS and SP angle-domain CIGs are shown in the mid-

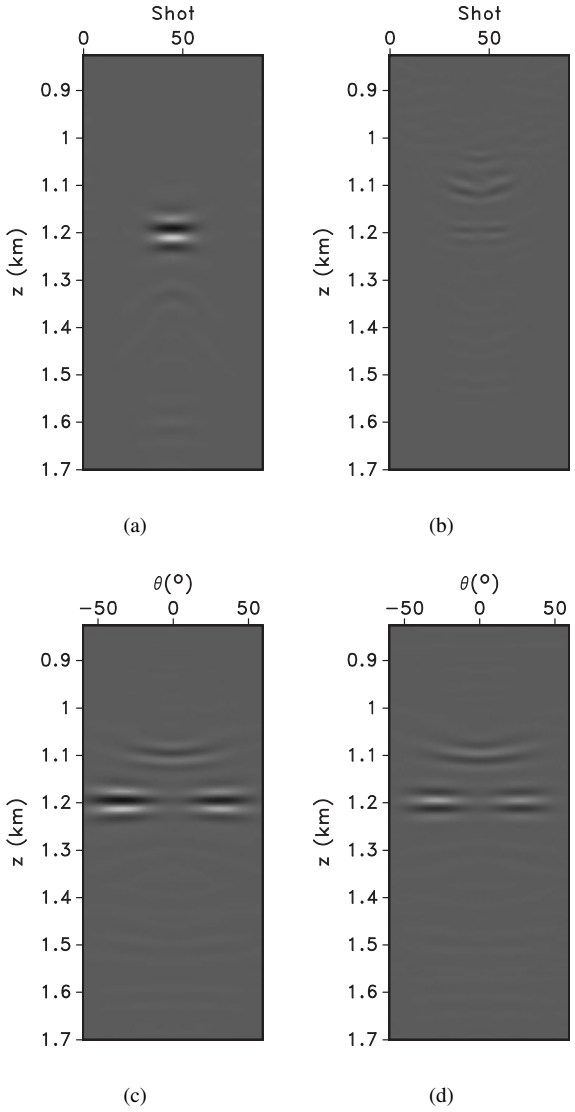
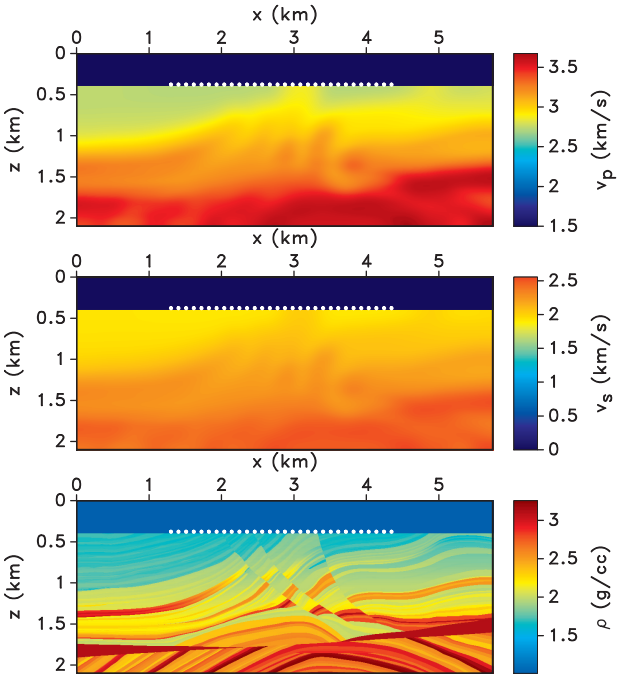


Figure 9. The (a) PP and (b) SS shot-domain CIG after artifact attenuation, and the (c) PS and (d) SP angle-domain CIG after artifact attenuation.



(a)

Figure 10. The Marmousi model; from top to bottom, the P velocity model, the S velocity model and the density model. The dots represent the locations of the OBS.

dle panels of Figures 12 and 13, respectively. Notice the vertical stripes caused by the sparse receivers used for migration. The events with nonzero energy near normal incidence with nonzero energy in the angle-domain CIGs are artifacts resulting from non-physical converted waves at the ocean bottom. The bottom panels of Figures 12 and 13 show the angle-domain CIGs after we reverse the polarity change and apply artifact attenuation. Artifact attenuation eliminates the non-horizontal artifacts but does not remove the artifacts from wave conversions that are flat near zero incidence angle.

By stacking the CIGs (bottom panels of Figures 11, 12, 13, and 14) over angle, we obtain the PP, PS, SP, and SS images shown from top to bottom in Figure 15. Note that the few remaining artifacts seen in the PS image are due to the limited number of shots used in migration. The SS image (bottom panel of Figure 15) is lower amplitude compared to the other three images because the energy of S waves, arising from P-to-S conversions, is much weaker to begin with. However, the events in the middle of the image appear very sharp because S-waves have shorter wavelength compared to P-waves due to their lower propagation velocity. The low wavenumber events in the left and right parts of the image are migrated from S diving waves, so they contain lower wavenumber content. These events are similar to the low-frequency backscattering artifacts seen in conventional RTM images.

This example demonstrates that elastic migration provides more information about the subsurface compared to acoustic migration. In addition to providing a PP image, which can be obtained using acoustic migration, elastic migration also provides PS, SP, and SS images. These additional images provide information about elastic reflection coefficients, which are related to subsurface material properties that and be used for reservoir characterization and petrophysical analysis. Also, PS, SP, and SS images can provide new geologic information, or they can simply provide added confirmation of structural information obtained from PP images.

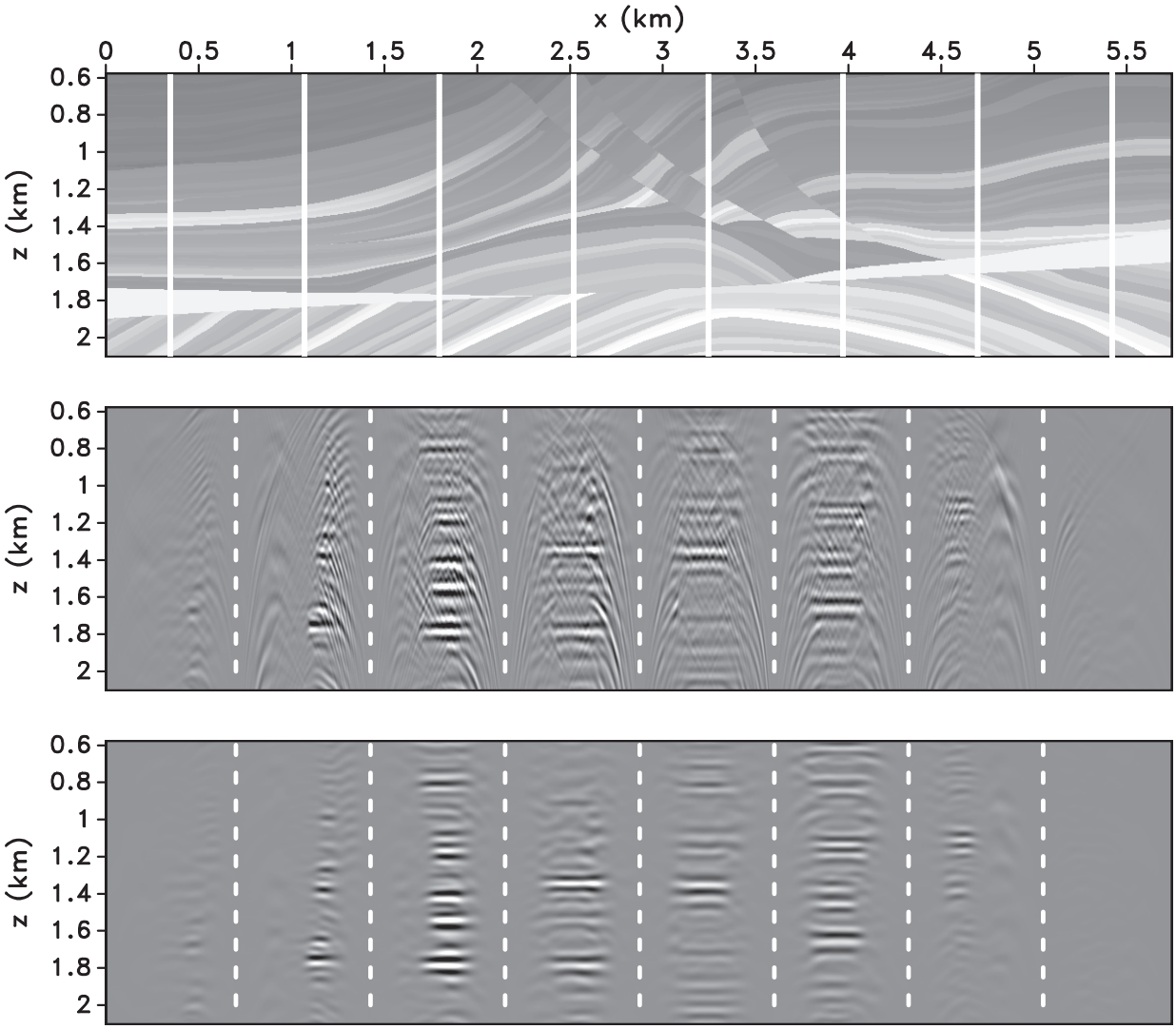


Figure 11. PP migration results, depicting from top to bottom the conventional image, and the angle gathers before and after artifact attenuation. The angles are ploted in the $\pm 75^\circ$ range.

4 CONCLUSIONS

We propose a method for elastic imaging using OBS first-order receiver-side multiples. These multiples carry additional information about the subsurface, but more data processing steps are needed in order to place the observed data at correct locations in the subsurface and to attenuate artifacts caused by non-physical conversions at the water bottom.

We use angle-domain CIGs to reverse the polarity change at normal incidence and to attenuate other artifacts due to sparse acquisition and non-physical wave conversions arising during wavefield reconstruction. We apply an f-k filter to attenuate the artifacts in CIGs while preserving amplitudes of the true events.

Our method is subject to several assumptions and limitations. We perform elastic migration by migrating only receiver-side first-order water-column multiples. Higher-order multiples were regarded as noise, as they are weaker than first-order multiples. However, if we could identify the higher-order multiples, they could also be used for elastic migration in order to obtain images with wider illumination. Also, during migration, we use a sharp liquid/solid boundary at the ocean bottom which enables the wave-modes to converse at the ocean bottom. Such a sharp liquid-solid boundary at the ocean bottom does not always exist, and as a result, converted S-modes may be weak; thus reducing our ability to exploit down-going converted modes.

However, the elastic images still provide complementary information about the subsurface, and can be used to infer additional geologic information and to perform more accurate petrophysical analysis compared to more conventional images

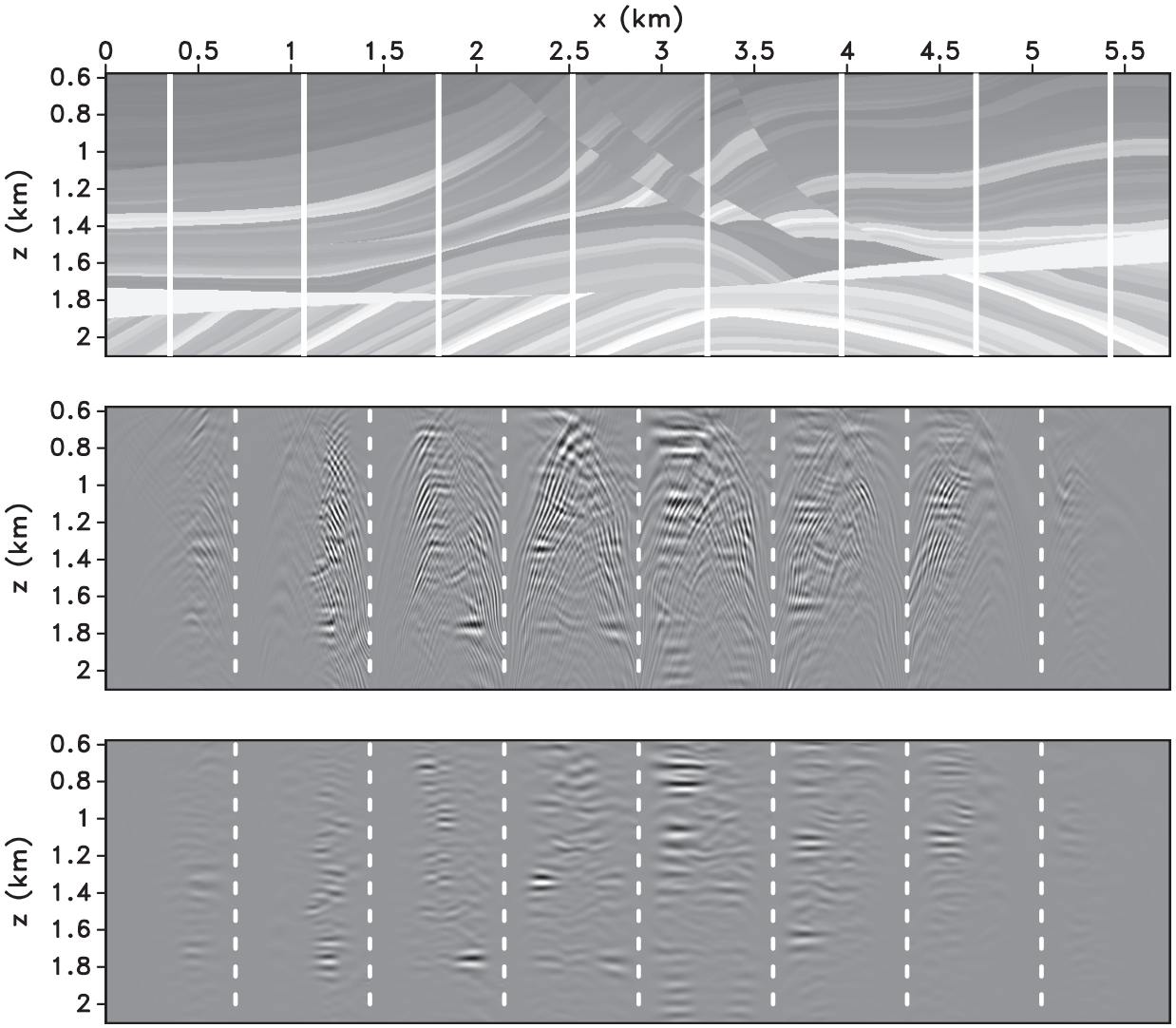


Figure 12. PS migration results, depicting from top to bottom the conventional image, and the angle gathers before and after artifact attenuation. The angles are ploted in the $\pm 75^\circ$ range.

obtained from acoustic data. The obtained elastic images are based on the physics of wave propagation and thus have clear physical meaning, which offers the potential for elastic velocity analysis.

5 ACKNOWLEDGMENTS

We thank sponsor companies of the Consortium Project on Seismic Inverse Methods for Complex Structures, whose support made this research possible. The reproducible numeric examples in this paper use the Madagascar open-source software package (Fomel et al., 2013) freely available from http://www.ahay.org.

REFERENCES

Aki, K., and P. Richards, 2002, Quantitative seismology (second edition): University Science Books.

Amundsen, L., and A. Reitan, 1995, Decomposition of multicomponent sea-floor data into upgoing and downgoing P- and S-waves: Geophysics, **60(2)**, 563–572.

Balch, A. H., and C. Erdemir, 1994, Sign-change correction for prestack migration of P-S converted wave reflections: Geophysical Prospecting, **42**, 637–663.

Barr, F. J., and J. L. Sanders, 1989, Attenuation of water-column reservations using pressure and velocity detectors in a water-bottom cable: 59th Annual International Meeting, SEG, Expanded Abstracts, 653–656.

Berg, E., C. Vuillermoz, G. Ekmann, and G. Woje, 2010, Origin and advances of the planted 4C seismic node technol-

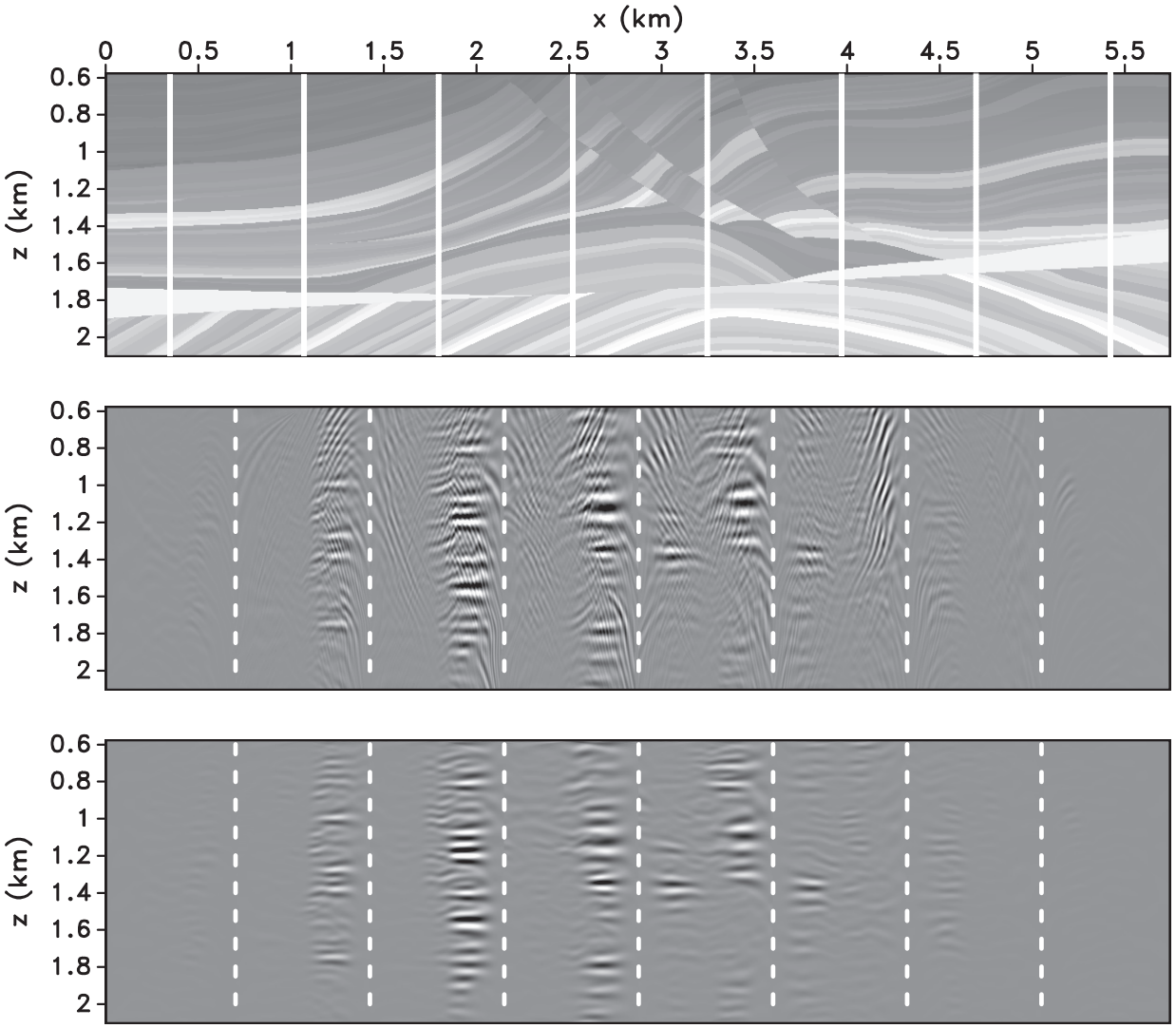


Figure 13. SP migration results, depicting from top to bottom the conventional image, and the angle gathers before and after artifact attenuation. The angles are ploted in the $\pm 75^\circ$ range.

ogy: 80th Annual International Meeting, SEG, Expanded Abstracts, 3728–3733.

Dash, R., G. Spence, R. Hyndman, S. Grion, Y. Wang, and S. Ronen, 2009, Wide-area imaging from OBS multiples: Geophysics, **74(6)**, Q41–Q47.

Dellinger, J., and J. Etgen, 1990, Wavefield separation in two-dimensional anisotropic media: Geophysicas, **55(7)**, 914–919.

Du, Q., Y. Zhu, and J. Ba, 2011, Polarity reversal correction for elastic reverse time migration: Geophysics, **77(2)**, S31–S41.

Fomel, S., 2002, Applications of plane-wave destruction filters: Geophysics, **67(6)**, 1946–1960.

Fomel, S., P. Sava, I. Vlad, Y. Liu, and V. Bashkardin, 2013, Madagascar: open-source software project for multidimensional data analysis and reproducible computational experiments: Journal of Open Research Software, **1**, e8.

Grion, S., R. Exley, M. Manin, X. Miao, A. Pica, Y. Wang, P. Granger, and S. Ronen, 2007, Mirror imaging of OBS data: First Break, **25**, 37–42.

Hoffe, B. H., P. W. Cary, and L. R. Lines, 1999, A simple and robust method for combining dual-sensor OBC data?: CREWES Research Report, **11**.

Jin, H., and P. Wang, 2012, Model-based Water-layer Demultiple (MWD) for shallow water: from streamer to OBS: 82th Annual International Meeting, SEG, Expanded Abstracts, 1–5.

Ma, J., M. K. Sen, X. Chen, and Y. Liu, 2010, Obc multiple attenuation technique using srme theory: 80th Annual International Meeting, SEG, Expanded Abstracts, 3473–3477.

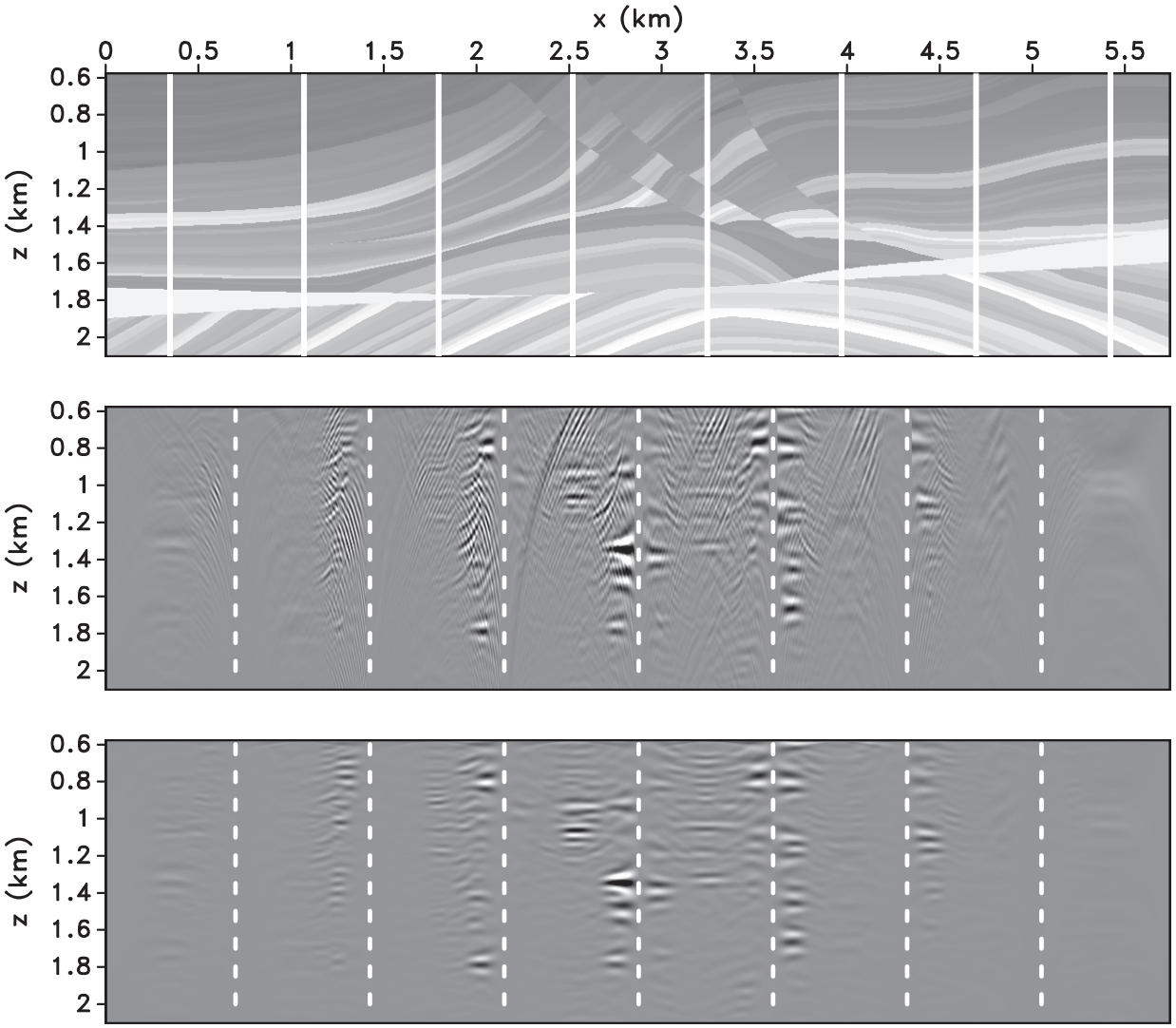


Figure 14. SS migration results, depicting from top to bottom the conventional image, and the angle gathers before and after artifact attenuation. The angles are ploted in the $\pm 75^{\circ}$ range.

O'Brien, J., B. Farmani, and B. Atkinson, 2013, VSP imaging using free-surface multiples: A case study from the Gulf of Mexico.: The Leading Edge, **32(10)**, 12581266.

Oppenheim, A. V., and R. W. Schafer, 2009, Discrete-time signal processing (3rd edition): Prentice Hall.

Osen, A., and L. Amundsen, 2001, Multidimensional multiple attenuation of obs data: 71th Annual International Meeting, SEG, Expanded Abstracts, 817–820.

Pica, A., M. Manin, P. Y. Granger, D. Martin, E. Suaudeau, B. David, G. Poulain, and P. Herrmann, 2006, 3D SRME on OBS data using waveform multiple modeling: 76th Annual International Meeting, SEG, Expanded Abstracts, 2659–2663.

Rickett, J. E., and P. C. Sava, 2002, Offset and angle-domain common image-point gathers for shot-profile migration: Geophysics, **67(3)**, 883–889.

Ronen, S., L. Comeaux, and X. Miao, 2005, Imaging Downgoing waves from Ocean Bottom Stations: 75th Annual International Meeting, SEG, Expanded Abstracts, 963–966.

Sava, P., and S. Fomel, 2003, Angle-domain common image gathers by wavefield continuation methods: Geophysics, **68**, 1065–1074.

Sava, P., and A. Guitton, 2005, Multiple attenuation in the image space: Geophysics, **70(1)**, V10–V20.

Sava, P., and I. Vlad, 2011, Wide-azimuth angle gathers for wave-equation migration: Geophysics, submitted for publication.

Sava, P. C., and I. Vasconcelos, 2009, Efficient computation of extended images by wavefield-based migration: SEG Technical Program Expanded Abstracts 2009, 2824–2828.

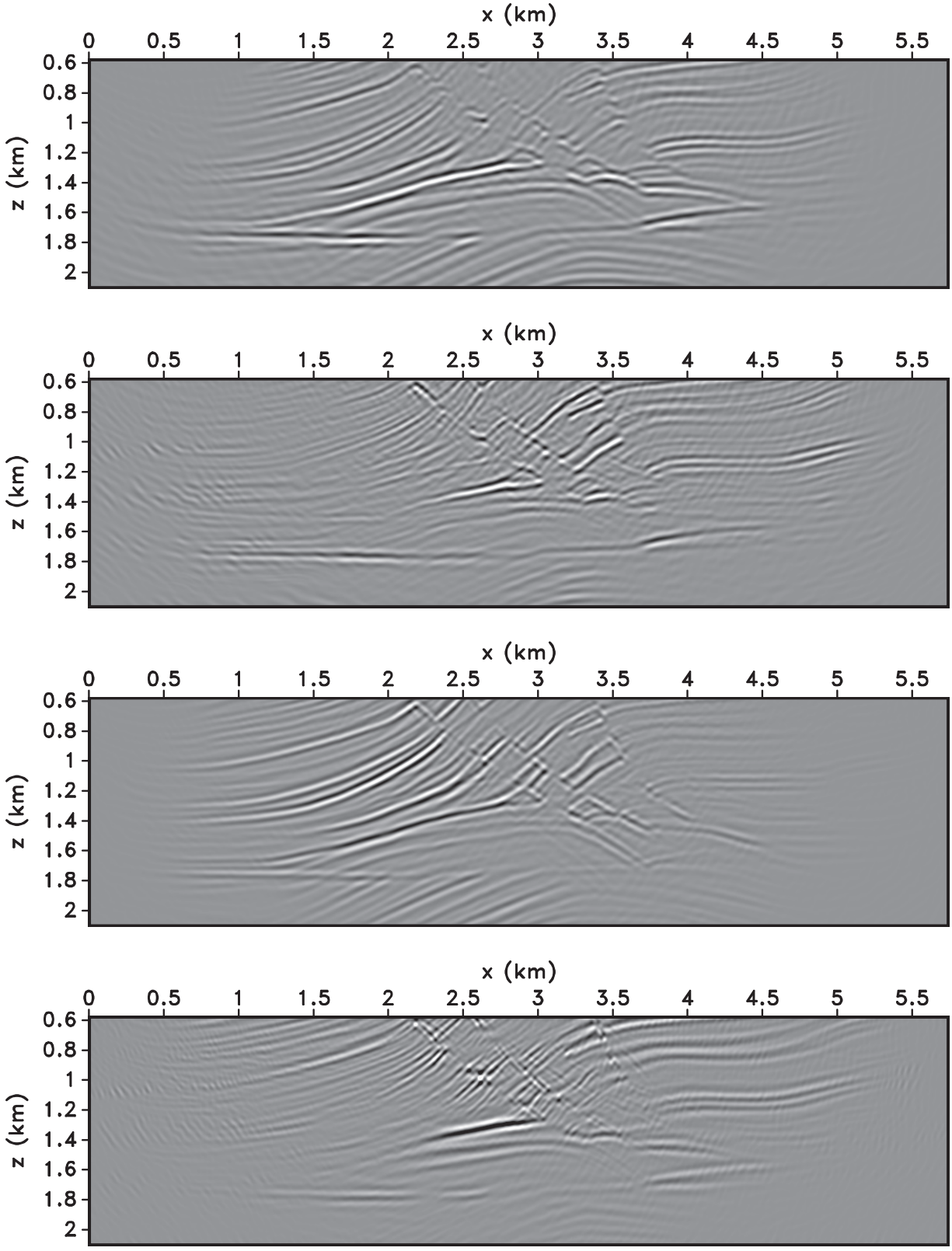


Figure 15. Migrated images for the Marmousi model. From top to bottom, the PP, PS, SP, and SS images, respectively.

Schalkwijk, K. M., 2001, Decomposition of multicomponent ocean-bottom data into P- and S-waves: PhD thesis, Delft University of Technology.

Stewart, R. R., and D. Schieck, 1989, 3-d F-K filtering: SEG Technical Program Expanded Abstracts 1989, 1123–1124.

Tu, N., T. Lin, and F. Herrmann, 2011, Migration with urface-related multiples from incomplete seismic data: 81st Annual International Meeting, SEG, Expanded Abstracts, 3222–3227.

Wong, M., S. Ronen, and B. Biondi, 2011, Least-squares reverse time migration/inversion for ocean bottom data: a case study: 81st Annual International Meeting, SEG, Expanded Abstracts, 2369–2373.

Xia, G., R. Clarke, J. Etgen, N. Kabir, K. Matson, and S. Michell, 2006, OBS multiple attenuation with application to the deepwater GOM Atlantis OBS nodes data: 76th Annual International Meeting, SEG, Expanded Abstracts, 2654–2658.

Yan, J., and P. Sava, 2008, Isotropic angle-domain elastic reverse-time migration: Geophysics, **73(6)**, S229S239.

Yan, R., and X.-B. Xie, 2012, An angle-domain imaging condition for elastic reverse time migration and its application to angle gather extraction: Geophysics, **77(5)**, S105–S115.